Crystallization process and glass stability of an $Fe_{48}Cr_{15}Mo_{14}C_{15}B_6Tm_2$ bulk metallic glass

Akihiko Hirata,[1,*] Yoshihiko Hirotsu,[1,2] Kenji Amiya,[3] and Akihisa Inoue[3]
[1]*Institute of Scientific and Industrial Research, Osaka University, Ibaraki, Osaka 567-0047, Japan*
[2]*R&D Institute of Metals and Composites for Future Industries (RIMCOF), Osaka University Laboratory, Ibaraki, Osaka 567-0047, Japan*
[3]*Institute for Materials Research, Tohoku University, Sendai 980-8577, Japan*
(Received 29 June 2008; revised manuscript received 9 September 2008; published 27 October 2008)

The crystallization process in an $Fe_{48}Cr_{15}Mo_{14}C_{15}B_6Tm_2$ metallic glass has been investigated by means of nanobeam and selected area electron-diffraction techniques. We found that the first crystallization reaction proceeds through a complicated nanoscale process, that is, amorphous $\rightarrow \chi$-FeCrMo-like long-period structures $\rightarrow \chi$-FeCrMo $\rightarrow M_{23}C_6$. A long-period structure began forming as an extended structure of medium range order; its periodicity gradually changed with the growing stage on annealing, and the structure finally changed into χ-FeCrMo. The common structural unit among these structures was found to be an atomic coordination polyhedron with a coordination number of 16. On the basis of the results, we discuss the phase stability of the $Fe_{48}Cr_{15}Mo_{14}C_{15}B_6Tm_2$ metallic glass as well as its local atomic arrangements.

DOI: 10.1103/PhysRevB.78.144205 PACS number(s): 64.70.pe, 64.70.dg, 61.05.jm

I. INTRODUCTION

In many multicomponent alloy systems, it has been found that glass states can be obtained even by using conventional casting methods with a slow cooling rate ($10^2 \sim 10^0$ K/s).[1] Such methods enable us to manufacture bulk metallic glasses (BMGs) that usually have centimeter-scale rod shapes. Numerous attempts have been made to understand the extremely high stability of the glass states from a structural viewpoint.[2] For example, in Zr-based BMGs, icosahedral atomic clusters have been suggested to exist in the glass states.[3,4] Because of the dense atomic packing of such clusters, atomic rearrangement becomes difficult, and therefore, the glass states have high stability. Interestingly, these icosahedral atomic clusters are identical to the main structural unit of the icosahedral quasicrystal and big-cube phase (Ti_2Ni-type) structures formed during the first crystallization process in several Zr-based BMGs.[3,5–9] This implies that there is a common and significant structural unit among the amorphous and crystalline states in each alloy system. Therefore, in order to understand the high stability of the glass state, it is necessary to examine the structural features of the amorphous state as well as the corresponding crystalline states in BMG systems.

Recently, in Fe-based alloys, a type of nonferromagnetic BMG with a large cross section of more than 1 cm has been fabricated using a Cu-mold casting method.[10–12] It was found that the glass-forming ability could be drastically improved by adding a small amount of Ln (lanthanides) to Fe-TM-ME alloys (TM: transition metal, ME: metalloid metal) such as Fe-(Cr, Mo)-(C, B) (Ref. 13) that exhibit a large supercooled liquid region before crystallization. One of the optimum chemical compositions for fabricating BMG rods with a diameter of more than 1 cm is $Fe_{48}Cr_{15}Mo_{14}C_{15}B_6(Ln)_2$.[10,12] Although it was reported that the crystalline product of these BMGs is basically the $M_{23}C_6$ phase (M: metal atom),[10,14] a detailed nanoscale structural observation has not yet been performed. In order to understand the extremely high glass stability of the different type of BMGs in terms of the common structural unit, in this paper, we present detailed analyses of the crystallization process, especially that of $Fe_{48}Cr_{15}Mo_{14}C_{15}B_6Tm_2$, by using selected area electron diffraction (SAED) and nanobeam electron diffraction (NBED). We specifically focus on structural changes in nanoscale regions as small as ~ 5 nm. NBED is a very powerful tool for determining atomic configurations in such nanoscale regions.

II. EXPERIMENTAL PROCEDURE

A ribbon and a rod of $Fe_{48}Cr_{15}Mo_{14}C_{15}B_6Tm_2$ metallic glasses were made by using the single-roll rapid quenching and Cu-mold casting techniques, respectively. In order to examine the crystallization process, the ribbon specimens were annealed isothermally at 893, 923, and 973 K for 30 min in a vacuum furnace. Specimens for TEM observation were prepared by electropolishing (using acetic-perchloric acid) at room temperature. The electropolished specimens were finally polished by using the Ar ion-milling technique at a voltage of 3 keV under a low glancing angle ($\sim 4°$) for a few minutes (GATAN PIPS). SAED patterns for structural analysis were taken by using a LEO-922D TEM (200 kV) equipped with an omega-type energy filter. NBED patterns were taken by using a JEM-3000F TEM (300 kV). The SAED patterns were recorded on imaging plates (IPs) and read by using an IP reader. NBED patterns were captured by using a TV-rate camera by scanning a nanoprobe (diameter: ~ 1 nm) on the specimen surface at a speed of ~ 10 nm/s. The electron dose at the nanoprobe was 2.0×10^{19} e/cm^2 (measured by using a Faraday gauge), almost ten times smaller than that for conventional high-resolution electron microscopy imaging. For each specimen, NBED patterns were captured from wide areas extending up to 0.5 mm in a continuous manner. We obtained more than 50 000 frames and selected approximately 100 frames with relatively clear net patterns for each specimen.

III. EXPERIMENTAL RESULTS

The differential scanning calorimetry (DSC) curves measured for both ribbon and 10 mm rod specimens at a heating

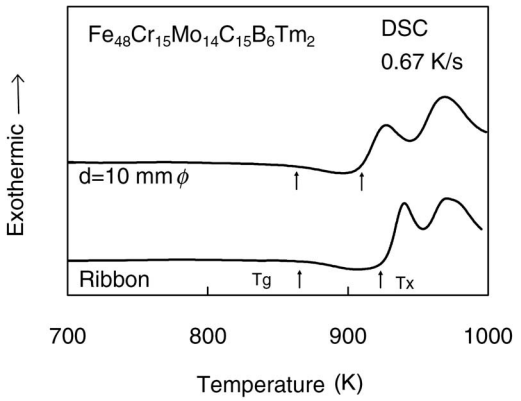

FIG. 1. DSC curves obtained from $Fe_{48}Cr_{15}Mo_{14}C_{15}B_6Tm_2$ (lower curve) ribbon and (upper curve) bulk specimens. The heating rate is 40 K/min.

rate of 40 K/min are shown in Fig. 1. The DSC curves indicated that the first crystallization reaction was divided into two different exothermic reactions. In addition, similar double exothermic reactions could be observed in both the profiles. Considering this result, we used the ribbon specimen for the TEM experiments in this study. The glass-transition temperature (T_g) and crystallization temperature (T_x) were approximately 865 (862) and 923 (914) K, respectively. This alloy exhibited a large supercooled liquid region having a temperature of approximately 58 (52) K. Note that the temperatures for the 10 mm rod specimen are given in the parentheses.

In order to understand the average information of the structural change, we took the SAED patterns of the as-quenched and annealed specimens. The SAED pattern for each specimen was taken using an energy-filtered TEM to eliminate the inelastic part of intensity. The SAED pattern shown in Fig. 2(a) was taken from the as-quenched specimen, whereas the patterns shown in Figs. 2(b)–2(d) were taken from specimens annealed at 893, 923, and 973 K, respectively, for 30 min. Note that the first exothermic reaction completes after annealing at 923 K for 30 min, whereas the second reaction completes after annealing at 973 K for 30 min. The halo rings observed in Fig. 2(a) are found to be sharpened in Fig. 2(b), and sharp diffraction spots begin to appear in Fig. 2(c). In Fig. 2(d), we can observe many distinct Debye rings; this indicates the formation of a polycrystalline microstructure.

From the SAED patterns shown in Fig. 2, we next calculated the total reduced interference functions [$Qi(Q)$]. Figure 3 shows four $Qi(Q)$ profiles obtained from the specimens annealed at 893, 923, and 973 K for 30 min and from the as-quenched specimen. Here, $i(Q)$ denotes the interference function, and Q is the scattering vector defined as $Q = 4\pi \sin\theta/\lambda$, where θ is the scattering angle and λ is the electron wavelength. A procedure for obtaining the $i(Q)$ curve from the SAED patterns has been described in our previous paper.[15] The $Qi(Q)$ profile of the as-quenched specimen was typical of that found in the case of amorphous alloys. In the profile at 973 K, we observed many sharp peaks that were obviously caused by a crystalline structure. For the purpose of comparison, a calculated $Qi(Q)$ profile

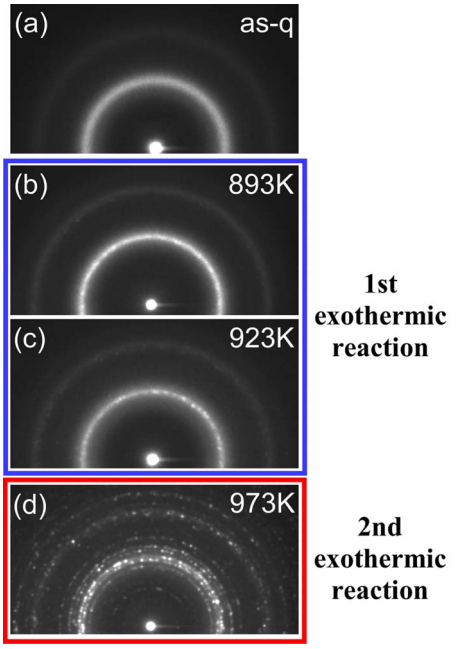

FIG. 2. (Color online) Energy-filtered SAED patterns obtained from (a) as-quenched specimen and specimens annealed at (b) 893, (c) 923, and (d) 973 K. The diameter of the selected area is approximately 400 nm. The SAED patterns after the (c) first and (d) second exothermic reactions in DSC.

obtained from an $M_{23}C_6$ [M: metal atom; prototype: cF116 $Cr_{23}C_6$ (Ref. 16)] crystal is also shown in the figure. All the peaks at 973 K were identical to those of the $M_{23}C_6$ structure. The lattice constant of the $M_{23}C_6$ structure used in the present calculation was 10.66 nm, as estimated from the present x-ray diffraction experiment using the specimen an-

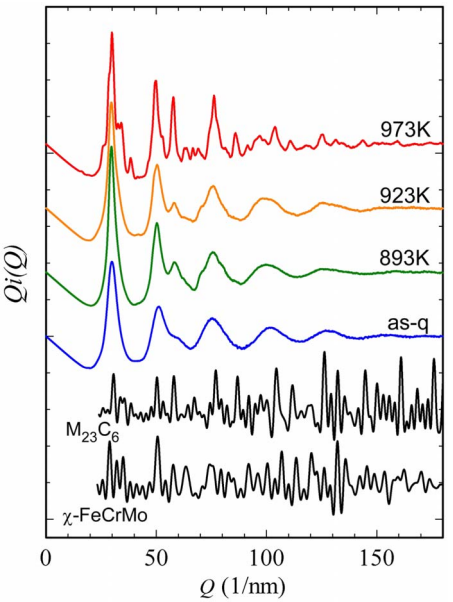

FIG. 3. (Color online) Reduced interference functions $Qi(Q)$ obtained from electron diffraction patterns of as-quenched and annealed specimens. Calculated $Qi(Q)$ profiles of the $M_{23}C_6$-type and χ-FeCrMo structures are also shown.

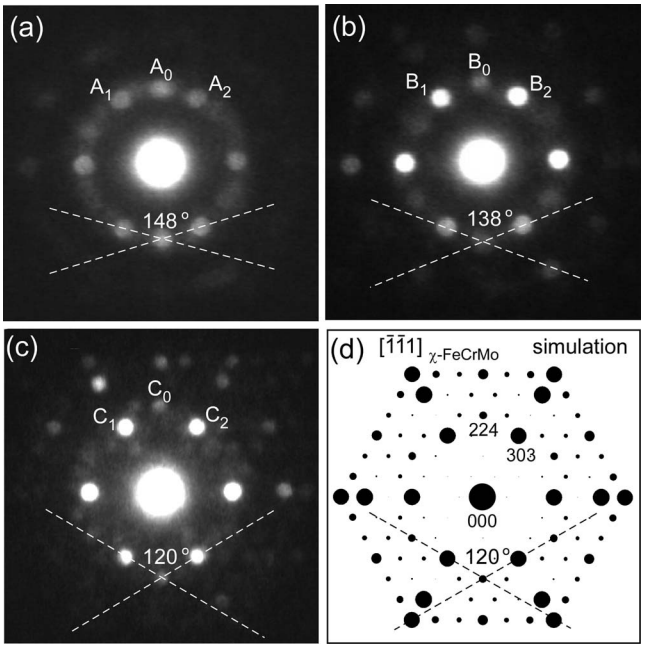

FIG. 4. NBED patterns captured from the specimens annealed at [(a) and (b)] 893 K and (c) 923 K along with a simulated diffraction pattern of χ-FeCrMo. The electron incidence of pattern (d) is parallel to the $[\bar{1}\bar{1}1]_{\chi\text{-FeCrMo}}$ direction. Pattern (c) is consistent with the simulated pattern, whereas patterns (a) and (b) are slightly different. The angles among three diffraction spots denoted by A_1-A_0-A_2, B_1-B_0-B_2, and C_1-C_0-C_2 are also shown in the figures.

nealed at 973 K. (The value for $Cr_{23}C_6$ found in the literature[16] is 10.65 nm; this value is similar to that obtained in the present x-ray experiment.) In contrast, shoulders of the peaks began to appear at temperatures above 893 K, indicating a structural change beyond this temperature. It was difficult to determine the structural details from only the $Qi(Q)$ profiles at 893 and 923 K.

A detailed study on the structural changes at 893 and 923 K was performed using NBED, and it was concluded that this change was due to a local structural development that led to the formation of a χ-FeCrMo phase. Figures 4(a)–4(c) show three experimental NBED patterns along with a calculated pattern obtained from a χ-FeCrMo structure (prototype: cI58 α-Mn) shown in pattern (d) [i.e., Fig. 4(d)]. Note that the χ-FeCrMo structure was first reported in a ternary Fe-CrMo alloy system,[17] and it was also found in Fe-X-C (X =Cr, Mo, or W) ternary alloys in which amorphous ribbons could be made by using a rapid quenching technique.[18] Patterns (a) and (b) were taken from the specimen annealed at 893 K, whereas pattern (c) was obtained from that annealed at 923 K. By comparing the experimental pattern (c) with the simulated one [pattern (d)], we found that pattern (c) was identified as that of the χ-FeCrMo structure (the electron incidence was parallel to the $[\bar{1}\bar{1}1]$ direction). On the basis of this observation, we also found that the shoulders in the $Qi(Q)$ profiles of the specimens annealed at 893 and 923 K were in good agreement with the peak positions of the calculated $Qi(Q)$ profile of χ-FeCrMo (see Fig. 3). In contrast, patterns (a) and (b) differed slightly from the perfect

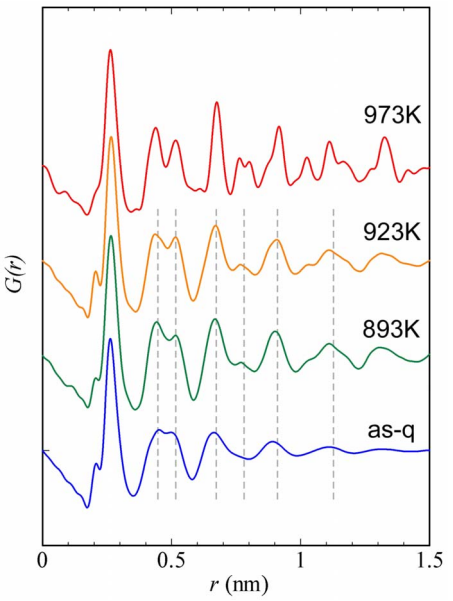

FIG. 5. (Color online) Reduced radial distribution functions $G(r)$ derived from the corresponding $Qi(Q)$ profiles of as-quenched and annealed specimens.

χ-FeCrMo pattern. In patterns (a) and (b), we can see the difference in 224-type reflections which positions approach the origin. As shown in the figures, the angles A_1-A_0-A_2, B_1-B_0-B_2, and C_1-C_0-C_2 are 148°, 138°, and 120°, respectively (the notations correspond to the three diffraction spots in each pattern). For a perfect χ-FeCrMo structure, a length of $4d_{224}$ almost coincides with the length of a [112] edge of the χ-FeCrMo unit cell projected on the $[\bar{1}\bar{1}1]$ plane. The angular shifts in patterns (a) and (b) could not be understood from the unit cell of the perfect χ-FeCrMo structure. We then assumed longer periodicities for these structures with a length of $8d_{224}$ (=1.47 nm) and $5.5d_{224}$ (=1.00 nm) along the [112] direction of the basic χ-FeCrMo structure for patterns (a) and (b), respectively. Consequently, this assumption enabled us to explain the angular shifts, that is, the positions of the strong spots A_0 and B_0. These results show that two types of long-period structures (LPSs) based on χ-FeCrMo can be stabilized in the initial stages of crystallization.

Figure 5 shows a series of reduced radial distribution functions $G(r)$ obtained from the as-quenched and annealed specimens. Each $G(r)$ profile corresponds to a $Qi(Q)$ profile with the same annealing temperature, as shown in Fig. 3. Details of the radial distribution function analysis method are described in our previous paper.[15] As seen in the figure, the oscillation in the profiles became clear with increasing temperature. Here, it should be noted that the peak-top positions are basically unchanged up to 923 K where the χ-FeCrMo structure (and LPS) is formed. This fact implies that the characteristics of one-dimensional projections of atomic correlations obtainable from $G(r)$ remained largely unchanged for annealing temperatures up to 923 K.

IV. DISCUSSION

In this study, we have investigated the crystallization process of $Fe_{48}Cr_{15}Mo_{14}C_{15}B_6Tm_2$, which belongs to a type of

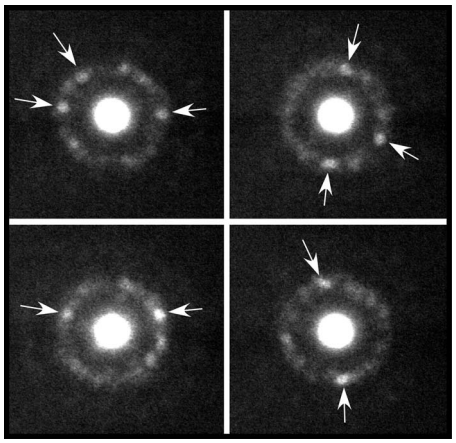

FIG. 6. Typical NBED patterns captured from the as-quenched specimen. The diffraction spots with strong intensity are frequently observed just on the first halo ring.

nonferromagnetic Fe-based BMG.[10–12] As mentioned above, the DSC curve during the first crystallization process was characterized by a double exothermic reaction. Here, it should be noted that the feature of the DSC curve for this alloy was basically the same as those in BMGs such as Fe-Cr-Mo-C-B-Er (Ref. 10) and Fe-Cr-Mo-Mn-C-B-Y (Ref. 11), which belong to the same BMG group. Moreover, in these BMGs, the $M_{23}C_6$ phase was found to mainly appear during the first crystallization process.[10,14] These facts suggest that the nanoscale structural development found in this study is also expected to occur in the same type of BMG and presumably provides a general understanding of the crystallization process in Fe-based BMGs.

The LPSs were found to appear in the initial stage of crystallization before the formation of χ-FeCrMo. Unfortunately, it is currently difficult to determine the atomic arrangements of LPSs because of their small sizes ($\sim$5 nm). However, the LPSs are presumably based on χ-FeCrMo because the characteristics of the NBED patterns of LPSs are similar to those of χ-FeCrMo. It is likely that the LPSs are similar to the α-Mn-like (α-Mn is a prototype of χ-FeCrMo) quasiperiodic structure already found in the Fe-B-Si-Nb alloy.[19] In addition, the $Qi(Q)$ profile at 893 K, where perfect χ-FeCrMo was hardly found, can be explained by using the χ-FeCrMo structure. Here, it should be noted that the χ-FeCrMo structure includes atomic coordination polyhedra with coordination numbers of 12, 13, and 16. Therefore, it is reasonable that the LPS structures also comprise coordination polyhedra with large coordination numbers, although their arrangements are different from that in χ-FeCrMo.

The formation of the local LPSs was found to precede the crystallization of χ-FeCrMo. Let us consider the relationship between the LPSs and the local atomic structures, especially medium range order (MRO), in the glass states. Figure 6 shows typical NBED patterns obtained from the as-quenched specimen. In these patterns, relatively sharp diffraction spots with strong intensity were found only on the first halo ring. Note that sharp diffraction spots could not be found in the simulated NBED patterns obtained from dense random packing structures.[15] Therefore, the strong reflections could be attributed to MRO structures as large as 1–2 nm.[15] We notice that with increasing periodicity of the LPSs, the position of the 224-type reflection approaches the peak-top position of the first halo ring (see Fig. 4). From the $G(r)$ profiles, it can be observed that the total atomic correlations of the as-quenched state were basically similar to those of the LPSs and the χ-FeCrMo structure. On the other hand, the NBED results revealed that the local ordered structures gradually change from MRO to χ-FeCrMo structures via the LPSs. Considering these results, we concluded that the MRO structures were more similar to the LPSs than to χ-FeCrMo (as well as $M_{23}C_6$).

When a nanosized χ-FeCrMo grain is formed, in the present system, surplus C and B atoms should be removed from the grain because the stoichiometric χ-FeCrMo phase does not contain these atoms. This implies that the composition of χ-FeCrMo differs from that of the glass state in the as-quenched specimen. In contrast, it is likely that the MRO regions have a composition similar to that of the glass state, and the LPSs have intermediate compositions lying between those of the glass state and χ-FeCrMo. From these assumptions, we could conclude that the formation of LPSs as well as MROs was attributable to an effort of the system that lowered the free energy without causing a large compositional change. The change in C and B contents on annealing induced a topological change in the atomic arrangements. Since the sizes of the C and B atoms were smaller than those of other metal atoms, these atoms form polyhedra with smaller coordination numbers; these polyhedra are probably identical to prism-type structures. The LPS or MRO formation was presumably due to the combination of polyhedra with large and small coordination numbers and their arrangements. According to a previous study,[20] the physical origin of LPS has been discussed in terms of the electron concentration or electrons per atom ratio (e/a). The LPSs based on the Laves phases comprising polyhedra with coordination numbers of 12 and 16 could be suitably explained in terms of the e/a value.[21] However, in the present case, the topological effect mentioned above is dominant because of the large size differences among the constituent atoms. For example, in the χ-FeCrMo and $M_{23}C_6$ structures, we could observe a difference in polyhedral arrangements with respect to the occupations of C and B atoms. Edge-shearing connections of the polyhedra with a coordination number of 16 were observed in $M_{23}C_6$ including C and B atoms, whereas face-shearing and intercrossed polyhedra were observed in χ-FeCrMo without C and B atoms (see Fig. 7). In the $M_{23}C_6$ structure, Archimedean antiprisms with central C and B atoms were formed connecting the polyhedra with a coordination number of 16.

In this study, several phases including χ-FeCrMo-like LPSs, χ-FeCrMo, and $M_{23}C_6$ as well as glass states with MRO were found in the course of the first crystallization reaction. Table I lists the phases found at each annealing stage and the number of nanoregions analyzed for each specimen. Note that when the NBED technique was used, a very small amount of χ-FeCrMo-like LPSs and χ-FeCrMo were found to remain in the specimen annealed at 973 K where the $M_{23}C_6$ phase was dominant. We could not find an additional phase in this specimen. Moreover, in the specimen

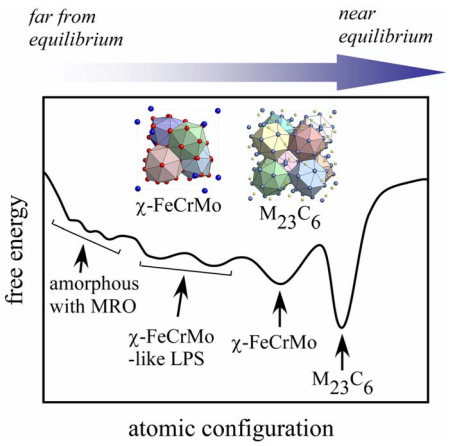

FIG. 7. (Color online) Conceptual diagram of stability for various atomic configurations in $Fe_{48}Cr_{15}Mo_{14}C_{15}B_6Tm_2$. The χ-FeCrMo and $M_{23}C_6$ structures including polyhedra with a coordination number of 16 are also shown in the inset.

annealed at 923 K, a small amount of $M_{23}C_6$ was also detected, although the dominant phases were χ-FeCrMo-like LPSs and χ-FeCrMo. From Table I, the sequence of structural development could be described as follows: amorphous structure with MRO $\rightarrow$ χ-FeCrMo-like LPSs $\rightarrow$ χ-FeCrMo $\rightarrow$ $M_{23}C_6$. Considering this order, we can depict a conceptual energy diagram with respect to the atomic configuration. In Fig. 7, there are some free-energy minima for the several states found in this study. With regard to the amorphous structures with MRO, some energy minima can be expected because there can exist some relaxed states, as is well known. The appearance of multiple states was directly related to that of various polyhedral configurations comprising polyhedra with large and small coordination numbers. The existence of several stable polyhedral configurations can presumably indicate the possibility of creating stable disordered atomic configurations, and therefore, the amorphous structures in BMG are considered to become stable.

TABLE I. Several phases found at each annealing stage and number of nanoregions analyzed for each specimen. Minor phases found in each specimen are shown in parentheses. The number of nanoregions corresponds to that of the clear NBED patterns selected from among more than 50 000 frames obtained using a TV camera.

Specimen	Phases found in each specimen	Number of nanoregions
as-quenched	amorphous with MRO	[a]
893 K; 30 min	χ-FeCrMo-like LPSs, amorphous with MRO	93
923 K; 30 min	χ-FeCrMo-like LPSs, χ-FeCrMo, amorphous with MRO, ($M_{23}C_6$)	163
973 K; 30 min	$M_{23}C_6$, (χ-FeCrMo-like LPSs, χ-FeCrMo)	103

[a]Strong reflections indicating the existence of MRO structures were always found in the NBED patterns obtained from the as-quenched specimen.

From the above-mentioned results, we consider that one of the common structural units in the different type of Fe-based BMG is coordination polyhedra with a large coordination number of 16. Very recently, Kazimirov *et al.*[22] examined the atomic structures for Fe-TM-(C,B)-Ln amorphous alloys using both neutron diffraction and *ab initio* computational techniques. For example, the alloy composition used in their calculation is $Fe_{63}Mo_{14}C_{15}B_6Er_2$, which is similar to that examined in this study. Characteristic atomic clusters such as the structural units of the glass were found in their realistic structural models. The coordination number of the atomic clusters around Fe atoms was approximately 13, whereas that around larger Mo atoms was approximately 15. It is interesting that the coordination numbers of glass were similar to those of χ-FeCrMo found in the present study. Note that according to the previous study,[17] the coordination numbers around Fe and Cr were 12 and 13, and those around Mo were 16 in χ-FeCrMo. The atomic clusters in glass were considered to be deformed or modified from the perfect ones in χ-FeCrMo because of the coexistence of the smaller C and B atoms and the larger Ln atoms. However, from the Voronoi polyhedron around Mo depicted in their paper, it appears that the basic feature of the clusters in glass was similar to that in χ-FeCrMo. In order to approach the atomic structure of glass experimentally, it is necessary to determine the atomic structure of the χ-FeCrMo-like LPS phases having structures more similar to the MRO structure in glass. It would be useful to compare the atomic structures of the LPS phases with the structural model obtained by using the *ab initio* calculation. Moreover, they also discussed the atomic diffusion derived from the atomic mean-square displacements. It was shown that Fe, C, and B atoms diffused considerably faster in the conventional $Fe_{79}C_{15}B_6$ amorphous alloy than in the BMG ($Fe_{49}Cr_{15}Mo_{14}C_{15}B_6Er_1$). This implies that the larger Mo or Ln atoms strongly influence the slowdown of the atomic diffusion of Fe, C, and B. It is also interesting how the slowdown correlates to the existence of the larger atomic clusters with the central Mo or Ln atoms.

The atomic structure of Zr-based BMG was also investigated by using *ab initio* molecular-dynamics simulation.[4] It was found that the icosahedral MRO structures mainly comprised intercross-shared icosahedra. In addition, edge-, vertex-, and face-shared icosahedra were also found in their structural model. From this result, it was concluded that icosahedral clusters are the main structural units in glass and they are interconnected in various manners. Note that intercross- and face-shared icosahedra can also be found in the big-cube (Ti_2Ni-type) crystalline phase[23] formed during the crystallization process of some Zr-based BMGs.[3,7] The various linkages of the icosahedral clusters in Zr-based alloys were somewhat similar to those of the large coordination polyhedra in the present alloy. Therefore, we can conclude that the existence of stable atomic clusters and their various stable linkages probably contribute to the high stability of the glass state in BMGs.

V. CONCLUSIONS

We examined the nanoscale structural change that occurs during the first crystallization reaction of

$Fe_{48}Cr_{15}Mo_{14}C_{15}B_6Tm_2$ by using electron diffraction techniques. We used the NBED technique to investigate the structural features of the nanoscale regions, and found it to be very useful. In this paper, we have presented a good example of the observation of nanoscale structures that vary from region to region. The structural change on annealing was as follows: amorphous structure with MRO $\rightarrow \chi$-FeCrMo-like LPSs $\rightarrow \chi$-FeCrMo $\rightarrow M_{23}C_6$. We found two types of χ-FeCrMo-like LPSs whose periodicities were 1.47 and 1.00 nm along the $\langle 224 \rangle_{\chi\text{-FeCrMo}}$-type direction. The common structural unit among the observed crystal structures was found to be an atomic coordination polyhedron with a coordination number of 16. The structural variation with the polyhedron was probably related to the high stability of the glass state. In addition, χ-FeCrMo gradually approached the MRO structures in the glass state with an increase in its periodicity. This implies that the MRO structures were more similar to the χ-FeCrMo-like LPSs than to χ-FeCrMo. The present alloy system exhibited a stepwise structural change on annealing, which led to the formation of multiple stable states including several polyhedral configurations. We believe that the high stability of the glass state in BMGs is attributable to the presence of multiple structural stabilities.

ACKNOWLEDGMENTS

This work was partly supported by the New Energy and Industrial Technology Development Organization under "Technological Development of Innovative Components Based on Enhanced Functionality Metallic Glass Composites" of Material Industrial Competitiveness Strengthening Program. A.H. would also like to sincerely thank A. Koreeda for his technical assistance.

*Corresponding author: ahirata@sankan.osaka-u.ac.jp

[1] A. Inoue, Acta Mater. **48**, 279 (2000).
[2] E. Matsubara and Y. Waseda, Mater. Trans., JIM **36**, 883 (1995).
[3] J. Saida and A. Inoue, J. Non-Cryst. Solids **317**, 97 (2003).
[4] X. Hui, H. Z. Fang, G. L. Chen, S. L. Shang, Y. Wang, and Z. K. Liu, Appl. Phys. Lett. **92**, 201913 (2008).
[5] U. Köster, J. Meinhardt, S. Roos, and H. Liebertz, Appl. Phys. Lett. **69**, 179 (1996).
[6] X.-P. Tang, J. F. Löffler, W. L. Johnson, and Y. Wu, J. Non-Cryst. Solids **317**, 118 (2003).
[7] I. Martin, T. Ohkubo, M. Ohnuma, B. Deconihout, and K. Hono, Acta Mater. **52**, 4427 (2004).
[8] K. Kajiwara, M. Ohnuma, T. Ohkubo, D. H. Ping, and K. Hono, Mater. Sci. Eng., A **738**, 375 (2004).
[9] M. Wollgarten, S. Mechler, E. Davidov, N. Wanderka, and M.-P. Macht, Intermetallics **12**, 1251 (2004).
[10] V. Ponnambalam, S. J. Poon, and G. J. Shiflet, J. Mater. Res. **19**, 1320 (2004).
[11] Z. P. Lu, C. T. Liu, J. R. Thompson, and W. D. Porter, Phys. Rev. Lett. **92**, 245503 (2004).
[12] K. Amiya and A. Inoue, Mater. Trans. **47**, 1615 (2006).
[13] S. Pang, T. Zhang, K. Asami, and A. Inoue, Mater. Trans. **42**, 376 (2001).
[14] H. J. Wang, G. L. Shiflet, S. J. Poon, K. Matsuda, and S. Ikeno, Appl. Phys. Lett. **91**, 141910 (2007).
[15] A. Hirata, Y. Hirotsu, T. Ohkubo, T. Hanada, and V. Z. Bengus, Phys. Rev. B **74**, 214206 (2006).
[16] A. L. Bowman, G. P. Arnold, E. K. Storms, and N. G. Nereson, Acta Crystallogr., Sect. B: Struct. Crystallogr. Cryst. Chem. **28**, 3102 (1972).
[17] J. S. Kasper, Acta Metall. **2**, 456 (1954).
[18] A. Inoue, T. Iwadachi, T. Minemura, and T. Masumoto, Trans. Jpn. Inst. Met. **22**, 197 (1981).
[19] I. V. Lyasotskii, N. B. Dyakonova, E. N. Vlasova, D. L. Dyakonov, and M. Y. Yazvitskii, Phys. Status Solidi A **203**, 259 (2006).
[20] H. Sato and R. S. Toth, Phys. Rev. **124**, 1833 (1961).
[21] Y. Komura, M. Mitarai, A. Nakaue, and S. Tsujimoto, Acta Crystallogr., Sect. B: Struct. Crystallogr. Cryst. Chem. **28**, 976 (1972).
[22] V. Y. Kazimirov, D. Louca, M. Widom, X.-J. Gu, S. J. Poon, and G. J. Shiflet, Phys. Rev. B **78**, 054112 (2008).
[23] G. A. Yurko, J. W. Barton, and J. G. Parr, Acta Crystallogr. **12**, 909 (1959).